Bioactive Materials 42 (2024) 270–283

Contents lists available at ScienceDirect

Bioactive Materials

journal homepage: www.keaipublishing.com/en/journals/bioactive-materials

Monascus pigment-protected bone marrow-derived stem cells for heart failure treatment

Tian Yue [a,1], Wentai Zhang [b,1], Haifeng Pei [c,1], Dunzhu Danzeng [d], Jian He [a], Jiali Yang [a], Yong Luo [a], Zhen Zhang [a], Shiqiang Xiong [a], Xiangbo Yang [e], Qisen Ji [e], Zhilu Yang [b,**], Jun Hou [a,*]

[a] Department of Cardiology, The Third People's Hospital of Chengdu/Affiliated Hospital of Southwest Jiaotong University, Chengdu Institute of Cardiovascular Disease, Chengdu, Sichuan, 610031, China
[b] Dongguan Key Laboratory of Smart Biomaterials and Regenerative Medicine, The Tenth Affiliated Hospital, Southern Medical University, Dongguan, Guangdong, 523000, China
[c] Department of Cardiology, The General Hospital of Western Theater Command, Chengdu, Sichuan, 610083, China
[d] School of Medicine, Tibet University, Lhasa, Tibet, 850000, China
[e] Ya'an Xunkang Pharmaceutical Co., LTD, Ya'an, Sichuan, 625015, China

ARTICLE INFO

Keywords:
BMSCs
Monascus pigment
Heart failure
Hydrogel
Microenvironment

ABSTRACT

Mesenchymal stem cells (MSCs) have demonstrated significant therapeutic potential in heart failure (HF) treatment. However, their clinical application is impeded by low retention rate and low cellular activity of MSCs caused by high inflammatory and reactive oxygen species (ROS) microenvironment. In this study, monascus pigment (MP) nanoparticle (PPM) was proposed for improving adverse microenvironment and assisting in transplantation of bone marrow-derived MSCs (BMSCs). Meanwhile, in order to load PPM and reduce the mechanical damage of BMSCs, injectable hydrogels based on Schiff base cross-linking were prepared. The PPM displays ROS-scavenging and macrophage phenotype-regulating capabilities, significantly enhancing BMSCs survival and activity in HF microenvironment. This hydrogel demonstrates superior biocompatibility, injectability, and tissue adhesion. With the synergistic effects of injectable, adhesive hydrogel and the microenvironment-modulating properties of MP, cardiac function was effectively improved in the pericardial sac of rats. Our results offer insights into advancing BMSCs-based HF therapies and their clinical applications.

1. Introduction

Heart failure (HF), the final stage of cardiac function decline, presents a significant challenge in advancing cardiovascular disease treatment [1,2]. Globally, approximately 32 million people suffer from HF, with a mortality rate of 15 %. The prognosis for this condition is bleak, imposing a substantial burden on families and society [3–5]. According to the *2022 AHA/ACC/HFSA* Guidelines *for the Management of Heart Failure*, treatment typically involves medications aimed at reducing cardiac load for preserving function, or surgical interventions. Despite recent reductions in HF mortality rates, current clinical treatments have not achieved complete cardiac regeneration, highlighting the urgent need for innovative therapies.

To restore cardiac function, researchers have proposed several new treatment strategies [6–10], with stem cell therapy showing great therapeutic value. Bone marrow-derived mesenchymal stem cells (BMSCs) are particularly promising due to their low immunogenicity capacity to differentiate, and paracrine effects that can promote tissue repair and regeneration [11–16]. However, challenges such as mechanical trauma during transplantation and the harsh

Peer review under responsibility of KeAi Communications Co., Ltd.
* Corresponding author. Department of Cardiology, The Third People's Hospital of Chengdu/Affiliated Hospital of Southwest Jiaotong University, Chengdu, Sichuan, 610031, China.
** Corresponding author. Dongguan Key Laboratory of Smart Biomaterials and Regenerative Medicine, Department of Cardiology, The Tenth Affiliated Hospital of Southern Medical University, Dongguan, Guangdong, 523059, China.
E-mail addresses: zhiluyang1029@smu.edu.cn (Z. Yang), houjun@swjtu.edu.cn (J. Hou).
[1] These authors contributed equally to this work.

https://doi.org/10.1016/j.bioactmat.2024.08.038
Received 27 July 2024; Received in revised form 29 August 2024; Accepted 29 August 2024

microenvironment rich in reactive oxygen species (ROS) and inflammation result in poor retention and survival rates of BMSCs [17–20], which significantly limited the clinical transformation of BMSCs therapies in treating HF. Furthermore, ROS and inflammation can continually exacerbate HF [21–23]. Studies highlight the pivotal role of ROS in cardiovascular disease, which activates signaling pathways involving nitric oxide and results in ventricular remodeling [24,25]. Moreover, persistent inflammation can increase apoptosis in cardiomyocytes, thereby increasing cardiac load and worsening cardiac function [21,23,26,27].

Restoring the cardiac microenvironment can protect heart tissue from long-term harm caused by ROS and inflammation, fostering conditions that improve BMSCs retention and survival [28–31]. In recent years, research has increasingly focused on developing biomaterials with ROS-scavenging capabilities to augment stem cell transplantation. However, these biomaterials have shown limited effectiveness in combating inflammation [18,32–34]. This limitation is particularly concerning because inflammation often exacerbates the adverse cardiac microenvironment following injury [35–38]. Notably, some of the active ingredients in traditional Chinese medicine have shown capacities to scavenge free radicals while ameliorating inflammation. Specifically, monascus pigment (MP), traditionally used as natural pigments for lowering blood lipids, have demonstrated additional benefits such as ROS-scavenging and inflammation-reducing properties [39–43], showing promising potential in treating cardiovascular disease.

Here, we developed an injectable, adhesive hydrogel (HY) containing MP nanoparticles (PPM) to enhance BMSC survival and function for HF cardiac regeneration (Fig. 1). Initially, HY was synthesized by crosslinking oxidized hyaluronic acid (OHA) and dopamine-modified hyaluronic acid (HADop) with carboxymethyl chitosan (CMC) via Schiff base [44]. The inclusion of dopamine, a bioinspired adhesive molecule, imparted strong adhesive properties to the HY, ensuring its attachment to myocardium. Subsequently, to increase the water solubility of MP and promote their uptakes by macrophages, MP were loaded with a polyethylene glycol-polycaprolactone (PEG-PCL, PP) polymer to form hydrophilic nanoparticle (PPM), which ameliorate the adverse microenvironment. Our findings demonstrate that PPM can restore the microenvironment, reduce oxidative stress in cardiomyocytes, decrease cardiomyocyte apoptosis, and sustain the secretory functions of transplanted BMSCs. Further animal studies confirmed that BMSCs transplanted within HY effectively promoted blood vessel growth, reduced fibrosis, and mitigated the detrimental effects of ventricular remodeling. These results offer valuable insights for advancing BMSCs-based therapies for HF.

2. Materials and methods

2.1. Synthesis of materials

Solvents used for synthesis are purchased from Chengdu Kelong Chemical Co., Ltd. To synthesize COOH-PEG-COOH, 10.00 g of PEG (Greagent, 011110094, Mw = 2000) was dissolved in chloroform and heated to 50 °C. Succinic anhydride (Macklin, S817605) and pyridine (Macklin, P837257) were then added, and the mixture was refluxed at 60 °C for 8 h. The reaction progress was monitored using thin-layer chromatography (TLC), and the solvent was subsequently removed by distillation. The resulting product was dissolved in dimethyl sulfoxide (DMSO), dialyzed against water (MWCO = 8000–14000) for 48 h, and then lyophilized to obtain COOH-PEG-COOH powder. To prepare 10.00 g ε-caprolactone (Aladdin, C109521), it was dissolved in benzyl alcohol (Macklin, B802542) with stannous chloride and vacuum-dried for 5 h at 30 °C. The mixture was then heated under vacuum to 140 °C for 6 h. After cooling, the product was dissolved in dichloromethane and stirred overnight. The product precipitated upon addition to ice-cold ethanol. After filtration and washing with ice-cold ethanol, the final product was obtained by drying. For synthesizing the PEG-PCL polymer, 1.60 g of COOH-PEG-COOH (0.68 mmol) was dissolved in 30 mL of dichloromethane. 133.9 mg Dicyclohexylcarbodiimide (DCC, TCI, D0436) was added, and the mixture was stirred for 15 min at room temperature. 3.20 g PCL and 79.30 mg 4-dimethylaminopyridine (DMAP, TCI, D1450) were then added, and the mixture was stirred under nitrogen at room temperature for 48 h. After confirming completion of the reaction by TLC, 2 mL of deionized water was added to stop the reaction. The resulting white solid was filtered, and the solvent was removed under reduced pressure. The residue was dissolved in 20 mL of ethyl acetate and cooled at 0 °C for 12 h. After filtration and collection, the product was distilled under reduced pressure and then precipitated in ice-cold ethanol. This purification process was repeated three times to obtain a

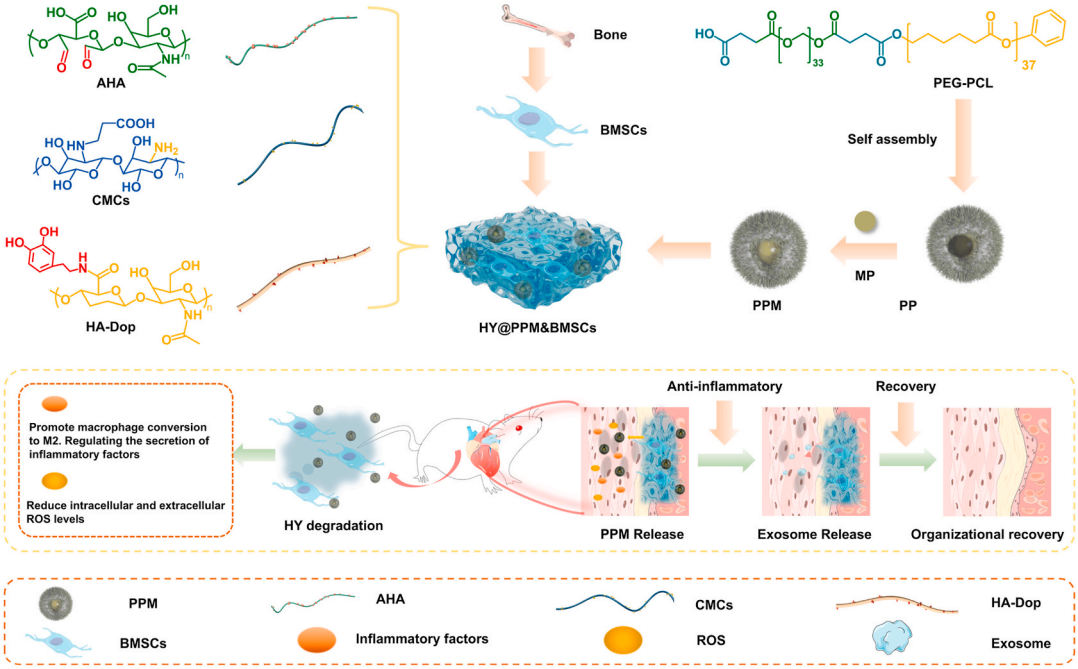

Fig. 1. Schematic design of the monascus pigments-encapsulated HY for BMSCs-based HF treatment.

white product, which was dried under low-temperature decompression to yield the PEG-PCL polymer.

To prepare OHA, 10.00 g of HA (Macklin, H909938, Mw = 800k-1500k) was dissolved in 90 mL of deionized water and stirred for 8 h until completely dissolved. Separately, 0.60 g of sodium periodate (Macklin, S817518) was dissolved in 10 mL of deionized water. This sodium periodate solution was added to the HA solution and allowed to react at room temperature for 5 h, protected from light. After the reaction, 1 mL of ethylene glycol was added, and the mixture was stirred for 30 min to stop the reaction. The solution was then dialyzed against deionized water for 48 h using a dialysis membrane (MWCO = 8000 to 14000), with regular water changes. Finally, the product was lyophilized to obtain OHA. For the synthesis of dopamine-modified hyaluronic acid (HA-Dop), 100 mg of HA was dissolved in water, and then 1-ethyl-3-(3-dimethylaminopropyl) carbodiimide hydrochloride (EDC-HCl, Bide Pharmatech, BD320671) and N-hydroxysuccinimide (NHS, TCI, M0018) were added to adjust the pH to 5. Dopamine hydrochloride in DMSO was added, and the mixture was stirred for 24 h. The resulting polydopamine spheres were filtered, and the solution was dialyzed against water (MWCO = 7000) for 72 h, with periodic water changes. The final product was obtained by lyophilizing the dialyzed solution.

To produce drug-loaded or blank nanoparticles, dissolve 10 mg of PEG-PCL in 10 mL of tetrahydrofuran (THF). If required, add 1 mg of MP to the solution. Slowly introduce the solution saline under stirring. Continue stirring until THF evaporates completely, forming nanoparticles. Dialyze these nanoparticles (MWCO = 1000) and then lyophilize to obtain the final product.

To create HY, first prepare 2.5 % solutions of OHA and HADop in saline, and a 5 % CMC solution at pH 7.4. Mix 5 mL each of the OHA and HADop solutions and let them stand for 5 min. Then, add 5 mL of the CMC solution and stir the mixture until an HY forms.

2.2. Characterization

^{1}HNMR (H Nuclear Magnetic Resonance Spectra, ASCEND 400), FT-IR (Fourier Transform Infrared Spectrometer, Nicolet 5700), nanoparticle size (Nano-ZS90), surface charge (Nano-ZS90), UV–Vis (Ultraviolet–visible spectra, UV2550), SEM (Scanning Electron Microscope, JSF 7800 Prime), and TEM (Transmission Electron Microscope, FEI, USA) analyses were performed following the respective equipment instructions.

To evaluate the antioxidant activity of PPM, a solution was prepared at 1 mg/mL and further diluted to concentrations of 100, 50, 25, and 10 μg/mL. The free radical scavenging efficiency (Dvc) of PPM was assessed using the DPPH assay, where Dvc (%) was calculated as $(A_{blank} - A_{positive\ control})/A_{blank} \times 100$ %.

The evaluation of HY included assessing gel formation time, injectability, and tissue adhesion. Initially, rhodamine B was introduced during HY preparation to track gelation time. Injectability was tested using a 26 G needle, followed by application to a knuckle and flexion 10 times to observe tissue adhesion effects after rinsing with SALINE buffer. Rheological properties of the HY were determined by preparing HYs in discs (diameter: 25 mm, thickness: 0.1 cm), maintaining a temperature of 37 °C, and analyzing the energy storage modulus and loss modulus across variations in angular frequency (0.1–100 rad/s).

Swelling and degradation of HY were assessed as follows: HY were placed in 50 mL centrifuge tubes at room temperature for 12 h to measure swelling. Then, 5 mL of deionized water was added to fully submerge the HY, and their weights were recorded at 37 °Cover various time points until equilibrium swelling was achieved and the weights stabilized.

Swelling percentage (%) = $(W_q - W_p)/W_p \times 100$ % W_p: initial weight of the gel (mg) W_q: weight of the gel at a specific time point (mg).

For degradation assessment, the HY were placed in 50 mL centrifuge tubes with 10 mL of phosphate buffer solution (PBS, pH 7.4) and agitated at 37 °C, 50 rpm. The gels were then subjected to lyophilization at various time intervals, and their weights were recorded to calculate the degradation percentage.

Degradation percentage (%) = $(W_0 - W_t)/W_t \times 100$ % W_0: initial weight of the gel (mg) W_t: weight of the gel at a specific time point (mg).

2.3. Cell culture, HF animal modeling and treatment

Unless otherwise specified, all reagents used in the cellular and animal experiments were purchased from Beijing EallBio Biomedical Technology Co., Ltd. H9c2 cells and RAW 264.7 cells (provided by Western Theatre General Hospital) were cultured in high-glucose DMEM with 10 % fetal bovine serum (FBS) and 1 % penicillin–streptomycin at 37 °C with 5 % CO_2. Macrophages were obtained from the peritoneal cavity of BALB/c mice (Male, 4–6 weeks, purchased from Chengdu Dossy Experimental Animals CO., LTD.) and cultured in RPMI-1640 medium supplemented with 10 % FBS and 1 % penicillin–streptomycin under the same conditions. BMSCs were isolated from SD rat (Male, 4–6 weeks, purchased from Chengdu Dossy Experimental Animals CO., LTD.) femoral bone marrow and cultured in DMEM/F12 medium with 10 % FBS and 1 % penicillin–streptomycin at 37 °C with 5 % CO_2.

An enhanced HF rat model was established by selecting SD rats with minor differences in body weight and dividing them into five groups: control, HF, HY@PPM, HY@BMSC, and HY@PPM&BMSC. To induce HF, 1.25 mg/kg Adriamycin (Meilunbio, MB1087) was administered intraperitoneally every 3–4 days for 6 weeks, totaling 15 mg/kg per rat [45]. The control group received equivalent volumes of saline. After establishing the model, three rats from each group underwent cardiac ultrasonography under anesthesia to assess changes in LVEDD, LVESD, and LVEF of the left ventricle. The success of the model was confirmed by an LVEF ≤60 % and overall rat condition. LVEF (%) was calculated as (LV end-diastolic volume - LV end-systolic volume)/LV end-diastolic volume × 100 %. For HF induction, rats were shaved one day prior to the experiment. Following anesthesia and assisted ventilation, the thoracic cavity was opened, and 100 μL/kg of the treatment agent was injected into the pericardium. The injection dosage was calculated as follow: Animal dose, μL/kg = (Cell dose, μg/mL × Liquid intake, mL)/(Animal weight, kg × Drug concentration, μg/μL). The entire procedure was conducted at 37 °C to maintain body temperature. The chest cavity was then closed with sutures, and rats were given 250 mg/kg penicillin intraperitoneally for three consecutive days. Treatment continued for 4 weeks from the time of administration.

2.4. Effect of PPM on inflammation

To induce M1 phenotype polarization in macrophages, 2×10^6 cells were seeded in 6-well plates and allowed to adhere for 4 h. The plates were then treated with 50 ng/mL LPS (MCE, HY-D1056) for 24 h. Following this, 3.86 μg/mL of either MP or PPM was added, and the cells were cultured for 72 h. Normal macrophages served as the control group. For cell staining analysis, macrophages were trypsin zed, washed thrice with PBS, and resuspended in 500 μL of PBS. From each sample, 200 μL of cell suspension underwent staining with all-negative (no antibody), mono-antibody, and all-positive antibody to differentiate negative and positive labeling. The remaining 300 μL was incubated with CD16/32 antibody, followed by CD11b (Cy 5.5), CD86 (PE), and isothiocyanate-labeled antibody buffer. After three PBS washes, cells were incubated with CD206 (FITC) for 30 min at 4 °C. Phenotypic changes in macrophages were assessed using flow cytometry (FC). The supernatant from macrophage cultures was collected and centrifuged at 4000 r/min for 10 min to remove insoluble particles. The secretion levels of TNF-α and IL-10 were quantified using an ELISA kit following manufacturer instructions. FC fluorescent dyes are purchased from Multisciences (Lianke) Biotech, Co., LTD.

2.5. Effect of PPM on cellular ROS and oxidative stress

2′,7′-Dichlorodihydrofluorescein diacetate (DCFH-DA, Macklin, D806685) serves as a widely used fluorescent probe for assessing intracellular ROS levels [46,47]. This probe enters cells by crossing the cell membrane and undergoes enzymatic hydrolysis, releasing DCFH. Upon exposure to ROS, DCFH is oxidized to generate the fluorescent compound DCF. To prepare for the experiment, H9c2 cells were seeded at a density of 2×10^5 cells per well in 6-well plates and allowed to reach 70 % confluence over 24 h. The culture medium was then replaced with 200 μM H_2O_2 to create a high-ROS environment. After 12 h, the medium was exchanged with blank nanoparticles, PPM, HY, or HY@PPM (each at a nanoparticle concentration of 100 μg/mL), and cells were further incubated for 12 h. Nuclei were stained with Hoechst 33342, and intracellular ROS levels were visualized using a fluorescence microscope. Cells were harvested using a trypsin digestion protocol, and intracellular ROS levels were quantified using FC.

2.6. Impact of the microenvironment on BMSCs

BMSCs were encapsulated in HY at a concentration of 1×10^6 cells/μL to prepare HY@BMSCs and HY@PPM&BMSCs, with PPM maintained at 50 μg/mL. A control group of BMSCs cultured under standard conditions without encapsulation was also included. CM-Dil (Yeasen, 40718ES50) labeling of BMSCs followed the manufacturer's instructions, and the 3D models were examined using fluorescence microscopy after 36 h of culture. CM-Dil fluorescence was detected at 553/570 nm (red), while MP fluorescence was measured at 425/530 nm (green). Cell viability was assessed using Cell Counting Kit-8 (CCK-8, Meilunbio, MA0225) assays on days 1, 3, 5, and 7. The HY was thoroughly mixed to ensure complete contact between cells and the CCK-8 solution during the assays. Additionally, VEGF levels in the culture medium were quantified using an ELISA kit on the same days to evaluate vascular growth factor content.

2.7. Cell coculture

Transwell chambers were utilized to coculture bone marrow-derived mesenchymal stem cells (BMSCs) in the upper chamber with H9c2 cardiomyocytes in the lower chamber, along with the addition of 200 μM H_2O_2. H9c2 cells cultured under normal conditions were used as the control group. RNA was extracted and purified from H9c2 cell, followed by reverse transcription. Then the samples were added to the Fluorescent Real-Time Quantitative Polymerase Chain Reaction (qPCR) system with primers (Table S2), real-time recording the fluorescence intensity of each cycle, from which the initial copy number of the target gene is calculated.

2.8. Western blot

H9c2 cells were lysed using RIPA buffer supplemented with protease inhibitors. Total proteins were separated via SDS–polyacrylamide gel electrophoresis (PAGE) and transferred onto a 0.2 μm polyvinylidene fluoride (PVDF) membrane. The membrane was then incubated overnight at 4 °C with an anti-HO-1 antibody (1:2000). After washing with TBST, a secondary antibody was applied and incubated for 4 h at room temperature. Protein bands were visualized post-washing with TBST, and their intensities were quantified using ImageJ software. To assess cytotoxicity, HY, PPM, MP, and H_2O_2 were tested using a CCK-8 kit and cell live/dead staining as per the manufacturer's instructions.

2.9. Histological evaluation

Following the treatment of the rats, heart tissues were collected and prepared into sections. Subsequently, the samples were subjected to H&E (Beyotime C0105S) and Masson (Beyotime C0189S) staining to analyze the structural aspects of the heart.

2.10. Immunofluorescence staining

After 28 days of treatment, the rats were euthanized, and their intact hearts were collected for paraffin sectioning. The sections were processed by baking, dewaxing, and antigen retrieval. Following this, they were incubated with 5 % blank goat serum at 37 °C for 30 min. The CD86 primary antibody or Annexin V-FITC (Yeasen, 40302ES50) was diluted according to the manufacturer's instructions and applied to the sections, followed by overnight incubation at 4 °C. After a 15 min rewarming step at room temperature, the sections underwent three washes with PBS to remove excess primary antibody. A secondary antibody working solution was prepared according to instructions, applied to the samples, and incubated for 1 h at room temperature in the dark. Subsequently, the samples were washed three times with PBS. The sections were then incubated with DAPI (2 μM) working solution for 15 min at room temperature in the dark. After removing the DAPI solution, the sections underwent three additional washes with PBS. Finally, the sections were sealed, fluorescence images were captured, and the fluorescence intensity was observed and quantified.

2.11. Echocardiography

After 28 days of treatment, the left ventricular function of the HF model mice and mice was evaluated using an ultrasound imaging system (Visual Sonic VEVO 2100).

2.12. Statistical analysis

The data obtained from the experiments are expressed as the mean ± standard deviation, and one-way ANOVA was used to analyze the differences between groups. Significance levels are denoted as $^*P \leq 0.05$, $^{**}P \leq 0.01$, $^{***}P \leq 0.001$, and $^{****}P \leq 0.0001$; when not specified, n = 3.

3. Results and discussion

3.1. Preparation and characterization of the PPM-encapsulated HY

The synthesis pathway of PP is depicted in Fig. 2A. Analysis using ^{1}HNMR revealed that the chemical shift at $\delta = 2.64$ ppm (d + e) corresponded to the proton resonance peaks of the two methylene groups adjacent to the carboxyl functional group, indicating successful grafting of the carboxyl group onto the polyethylene glycol (PEG) backbone (Fig. S1A). Additionally, the proton resonance peak at $\delta = 5.13$ ppm (b + c + d) was attributed to the aromatic protons of the benzene ring. Peaks observed at $\delta = 4.08$ ppm (i), $\delta = 2.33$ ppm (e), $\delta = 1.67$ ppm (f + h), and $\delta = 1.40$ ppm (g) were characteristic of the methylene groups within the polycaprolactone (PCL) main chain, confirming successful PCL polymerization (Fig. S1B). The integration of methylene proton peaks associated with the benzyl group (a) and those in the PCL main chain allowed the determination of the molecular weight of the PCL segment, estimated at approximately 4218 ± 316. Distinct proton resonance peaks for the benzene ring at $\delta = 7.37$ ppm (a+b) and a methylene peak at $\delta = 3.66$ ppm (i + j) corresponding to the PEG backbone further verified the successful synthesis of the PP graft copolymer (Fig. S1C). FT-IR analysis provided additional confirmation. The presence of a strong absorption band at 1567 cm^{-1}, indicative of C=O stretching vibrations, confirmed the successful addition of the carboxyl group to the PEG backbone (Fig. 2B). Moreover, the absorption peak at 2944 cm^{-1}, attributed to asymmetric methylene stretching vibrations, supported the polymerization of PCL. Furthermore, distinct absorption features of PCL and the presence of a C-O-C stretching vibration peak at 1095 cm^{-1} specific to the PEG backbone were observed in the PP copolymer, reinforcing its successful synthesis.

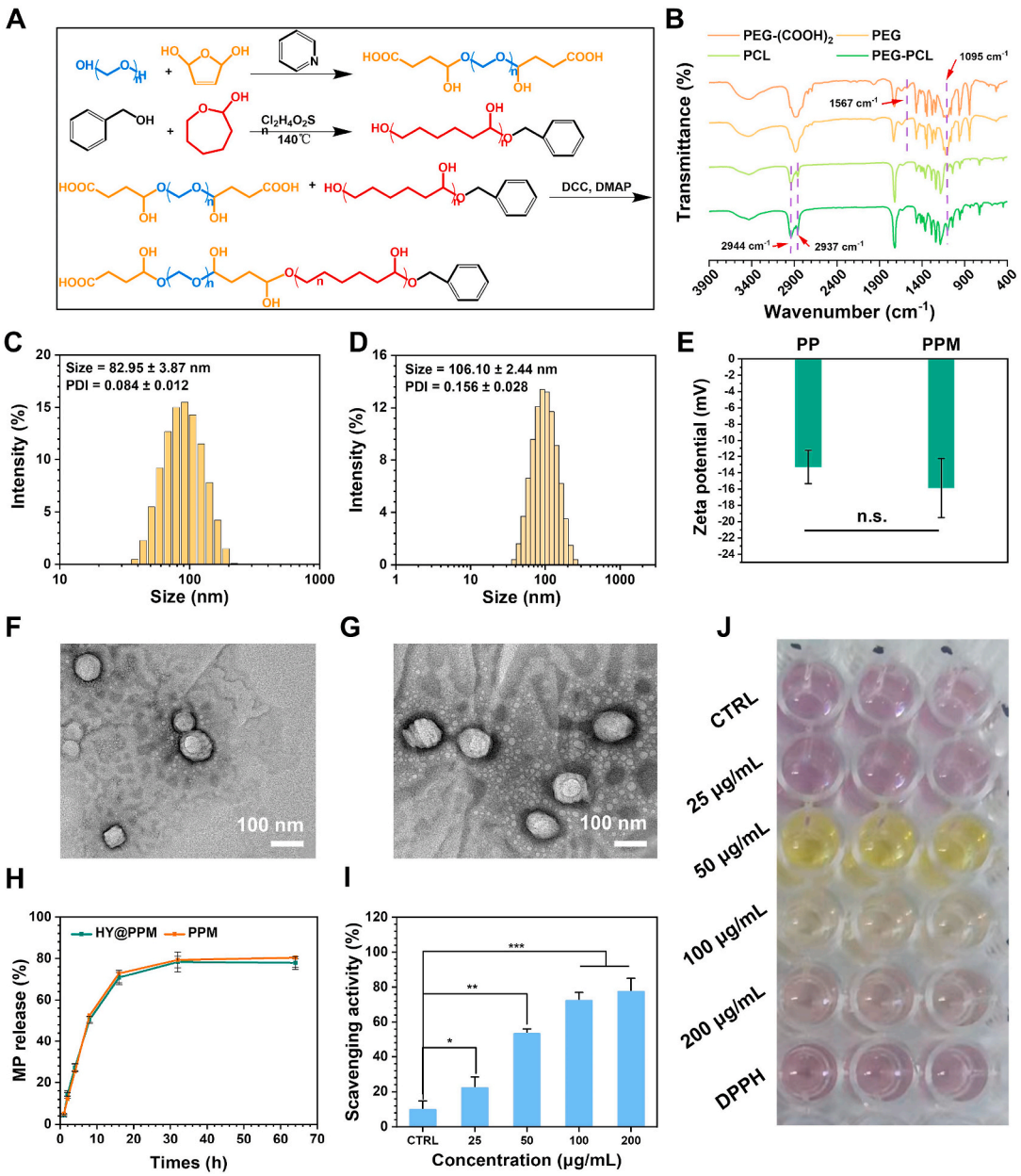

Fig. 2. (A) Synthesis pathway of PEG-PCL. (B) FT-IR spectra of COOH-PEG-COOH, PEG, PCL, and PEG-PCL. Particle size of (C) PP and (D) PPM. (E) Zeta potential of PP and PPM. TEM image of (E) PP and (F) PPM. (H) MP release profile of PPM and HY@PPM; (I–J) Free radical scavenging ability of MP particles at different concentrations.

Both blank and drug-loaded nanoparticles were synthesized for direct comparison. The results indicated that the sizes of the blank and drug-loaded nanoparticles were 82.95 ± 3.87 nm and 106.10 ± 2.44 nm, respectively (Fig. 2C and D). PPM had a negative surface charge (Fig. 2E), which is beneficial for minimizing potential cytotoxicity. TEM analysis further verified that PPM exhibited a uniform spherical shape and similar size compared to PP (Fig. 2F and G). UV–Vis spectroscopy revealed that the MP content in PPM was 7.72 ± 0.37 % (Table S1). The release kinetics of MP from PPM indicated an initial rapid release, with 60 % of the total MP released within the first 15 h (Fig. 2H). Notably, the release profiles of MP from HY@PPM and PPM were similar. 1,1-Diphenyl-2-picrylhydrazine (DPPH) radical scavenging experiments demonstrated that PPM effectively scavenged ROS (Fig. 2I and J). The scavenging efficacy of PPM increased with concentration, but no significant improvement was observed beyond 100 μg/mL.

Fig. 3A illustrates the synthesis pathway for the precursor materials of the HY. FT-IR analysis was conducted on both OHA and the resulting crosslinked HY. OHA showed a distinct absorption peak at 1724 cm^{-1}, indicating the conversion of ortho-dihydroxyl groups to aldehyde groups through C=O stretching vibrations (Fig. 3B). In the case of CMC, absorption peaks at 3488 cm^{-1} and 3411 cm^{-1} corresponded to amino groups within the CMC structure. The absorption peak at 749 cm^{-1}, associated with the benzene ring, confirmed the successful grafting of dopamine onto the polymer backbone. Following HY formation, the characteristic absorptions of amino and aldehyde groups were absent, indicating crosslinking of the HY through Schiff base reactions.

HY formation would occurs efficiently within approximately 90 ± 10 s after mixing the components (Fig. 3C). This rapid gelation time ensures that HY possesses good injectability. Given the dynamic environment of myocardium, it is crucial to develop HY with robust tissue adhesion and mechanical properties to retain BMSCs and PPM in the pericardium. Our HY was tested for tissue adhesion efficacy and

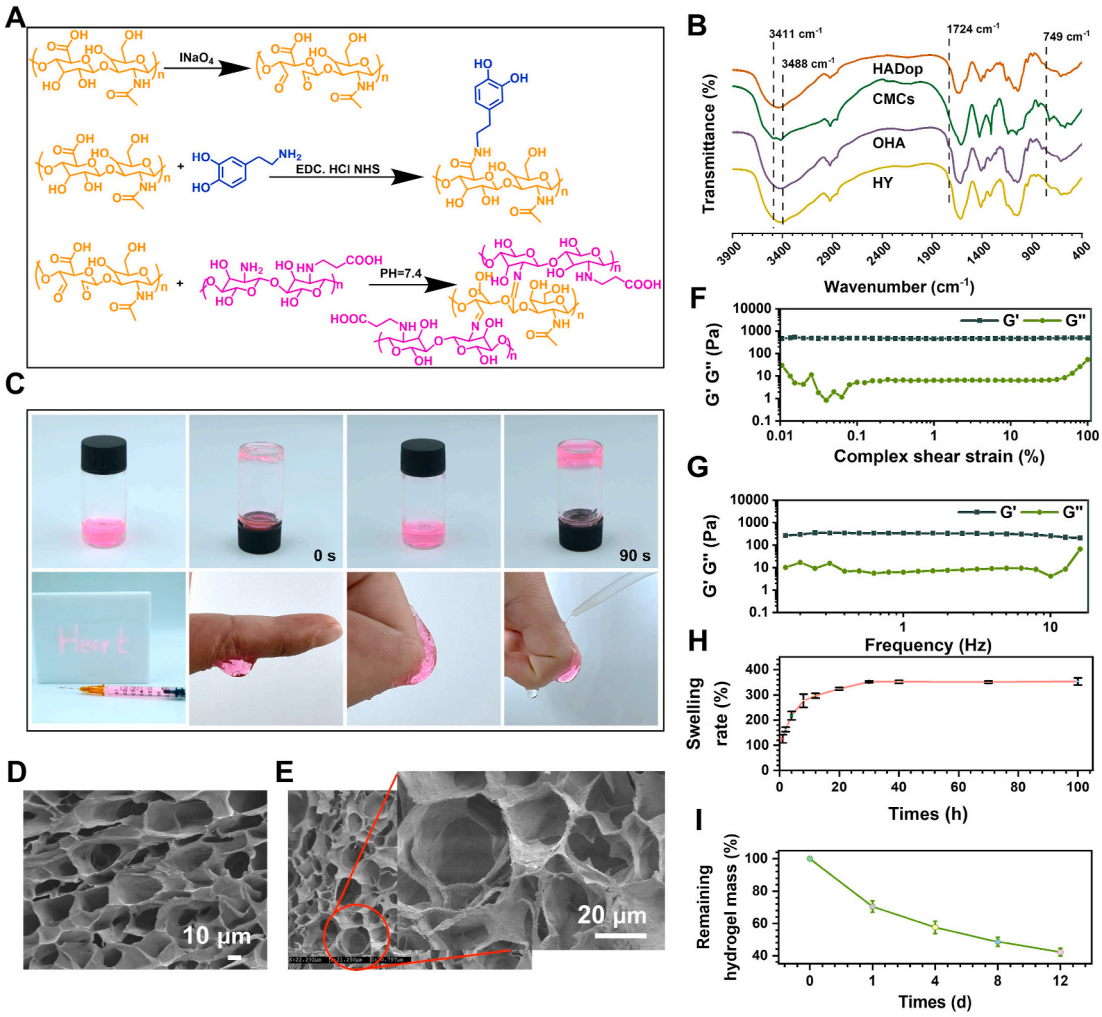

Fig. 3. (A) Synthesis pathways of OHA, HADop, and HY. (B) FT-IR spectra of HADop, OHA, CMC, and HY. (C) Gelation behavior, injectability and tissue adhesion of HY. SEM images of (D) HY and (E) HY@PPM. (F–G) Rheological properties of HY. (H) Swelling rate of HY. (I) Degradation behavior of HY.

demonstrated strong attachment even after flexing and exposure to water, indicating its ability to maintain adhesion in physiological conditions. SEM analysis of the HY surface revealed a porous structure with void sizes ranging from 10 to 50 μm (Fig. 3D), facilitating the embedding of PPM nanoparticles within these voids (Fig. 3E). Rheological characterization of HY using discs of 25 mm diameter and 0.1 cm thickness showed a predominance of elastic behavior over the frequency range of 0–10 Hz, with the energy storage modulus (G′) consistently higher than the loss modulus (G″) (Fig. 3F). Further assessment of G′ and G″ across a range of shear strains from 0.01 % to 100 % at a fixed frequency of 1 Hz demonstrated HY's ability to maintain its gel state under extensive deformation (Fig. 3G). Swelling experiments indicated that HY achieved a swelling ratio of 327 ± 10.5 % at 37 °C upon reaching equilibrium with saline (Fig. 3H). Additionally, the HY exhibited a degradation rate of 54.22 ± 5.28 % after 12 days (Fig. 3I). These findings underscore HY's suitability for biomedical applications requiring both mechanical robustness and biodegradability.

3.2. *PPM-encapsulated HY ameliorate the inflammatory microenvironment*

Prior to investigating the impact of HY@PPM on improving cardiac microenvironment, it was crucial to assess the cytotoxicity of both PPM and HY. This assessment involved testing their effects on two cell lines, H9c2 and RAW 264.7. Furthermore, concentrations of H_2O_2 were optimized using the H9c2 cell line to replicate conditions of increased ROS. Cytotoxicity experiments revealed that neither PPM nor HY at concentrations up to 200 μg/mL had significant toxic effects on the cells (Figs. S2A–C). However, cell viability began to decrease when the MP concentration exceeded 25 μg/mL and the H_2O_2 concentration exceeded 200 μM (Figs. S2D and E). Therefore, a concentration of 200 μM H_2O_2 was utilized to establish a high-ROS environment for subsequent experiments. Subsequently, the uptake of PPM by macrophages was examined. The results demonstrated a significant increase in the percentage of cells positive for intracellular MP, rising from 11.90 ± 0.07 % with MP alone to 21.71 ± 0.25 % with PPM (Fig. 4A–C). This improvement indicates that the nanoplatforms effectively enhanced the efficiency of MP utilization and their uptake by macrophages. The high surface area to volume ratio of nanoparticles enhances their interaction with macrophage receptors, boosting phagocytic activity. Additionally, their nanoscale size allows nanoparticles to mimic pathogens, making it easier for macrophages to recognize and engulf them as foreign objects [48,49]. Interestingly, there was no noticeable difference in the amount of internalized MP between the PPM and HY@PPM groups. This observation suggests that the presence of HY encapsulation around PPM does not influence the cellular phagocytosis of MP.

The balance of macrophage phenotypes is crucial in managing inflammation, particularly by transitioning from M1 (pro-inflammatory) to M2 (anti-inflammatory) states, thereby mitigating excessive inflammation [14,26,50,51]. In this study, lipopolysaccharide (LPS) was used

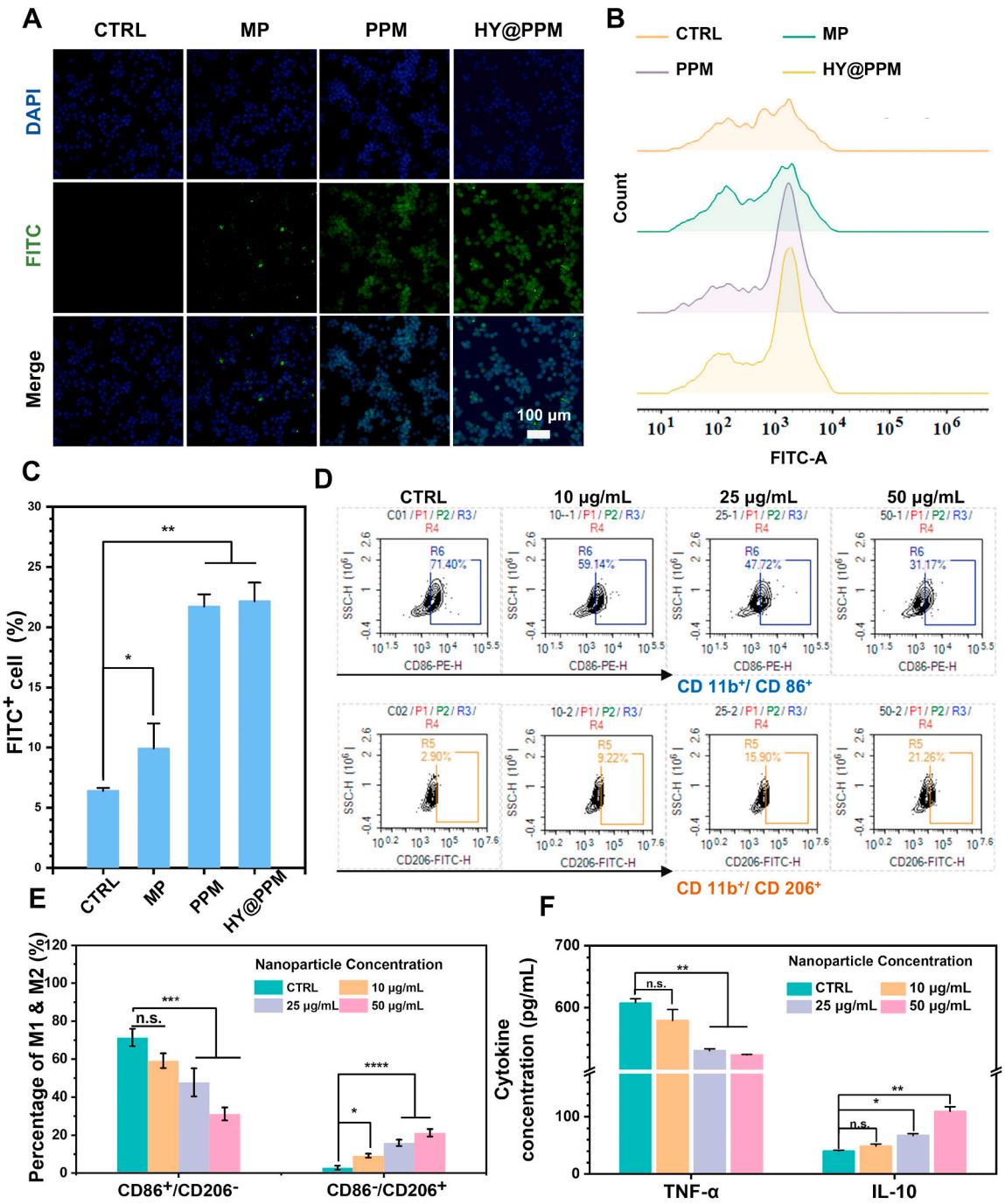

Fig. 4. (A) Macrophage phagocytosis according to the MP fluorogram. (B–C) FC results and statistics of macrophage phagocytosis of MP. (D–E) FC results and statistics of macrophage phenotypes. (F) ELISA analysis of TNF-α and IL-10 secretion by macrophages.

to induce a predominantly M1 phenotype, simulating hyper-inflammatory conditions. Flow cytometry analysis revealed that under LPS stimulation, M1 macrophages ($CD86^+/CD206^-$) constituted 70.23 ± 2.61 %, while M2 macrophages ($CD86^-/CD206^+$) accounted for 2.81 ± 1.62 %. Increasing concentrations of PPM led to a noticeable shift from M1 to M2 phenotype. At 50 μg/mL, PPM significantly reduced the $CD86^+/CD206^-$ ratio to 32.16 ± 1.55 % and increased the $CD86^-/CD206^+$ ratio to 20.26 ± 2.03 % (Fig. 4D and E). ELISA confirmed these findings, showing that increasing PPM concentration from 25 μg/mL to 50 μg/mL significantly reduced TNF-α and increased IL-10 secretion (Fig. 4F). No additional benefits were observed at 100 μg/mL. Hence, 50 μg/mL of PPM was identified as the optimal concentration for subsequent studies.

Moreover, increased intracellular ROS levels can initiate prolonged apoptosis in cardiomyocytes and activate various inflammatory cells, thereby exacerbating cardiac dysfunction [51,52]. Consequently, we also examined the ROS-scavenging abilities of PPM. DCFH-DA staining revealed significantly elevated intracellular ROS levels (green fluorescence) in H9c2 cells cultured under high-ROS conditions (Fig. 5A). While PP alone had minimal impact, PPM effectively reduced intracellular ROS levels upon MP introduction. Flow cytometry analysis indicated an increase in the percentage of ROS-positive cells from 11.99 ± 0.26 % to 37.13 ± 0.48 % under high-ROS conditions (Fig. 5B and C). Treatment with PPM decreased the percentage of ROS-positive cells to 22.46 ± 2.58 %, demonstrating its efficacy in mitigating elevated ROS levels. Notably, HY@PPM, incorporating HY components with

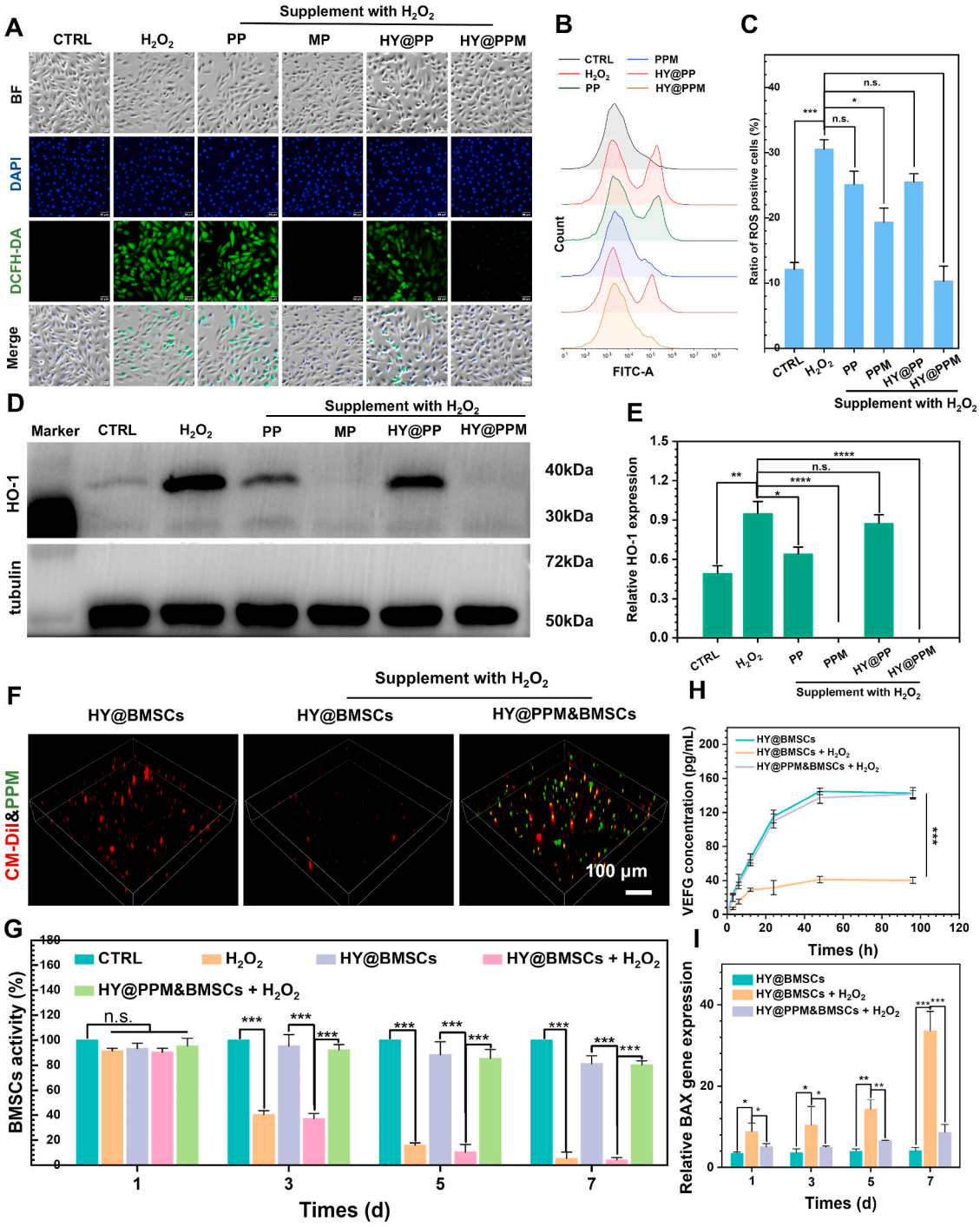

Fig. 5. (A) DCFH-DA fluorescence assay of ROS in H9c2 cells. (B–C) FC assay results and statistics of ROS in H9c2 cells. (D) Results of WB analysis of HO-1 protein expression in H9c2 cells. (E) Statistics of HO-1 protein expression in H9c2 cells (quantitative statistics using tubulin as a control). (F) Fluorescence 3-D modeling of the distribution of HY@BMSCs and HY@PPM&BMSCs under normal and ROS conditions. (G) Activity of HY@BMSCs as well as HY@PPM in normal and ROS environments for 1–7 days. (H) Effect of PPM on the VEGF secretion of BMSCs in adverse microenvironments. (I) Expression of the BAX gene after 1–7 days of coculture of BMSCs with H9c2 cells.

ROS-scavenging properties, further reduced ROS levels to nearly normal levels of 13.00 ± 0.44 %. Additionally, we assessed the expression of heme oxygenase-1 (HO-1), a pivotal enzyme in oxidative stress defense. The findings showed a significant increase in HO-1 expression under oxidative stress conditions, consistent with the rise in intracellular ROS levels observed via WB analysis (Fig. 5D and E). PPM notably alleviated oxidative stress in H9c2 cells, and this effect persisted post-encapsulation.

The BMSCs were harvested and cultured up to the P3 generation before being encapsulated in either HY or HY@PPM. Laser confocal microscopy was used to visualize the distribution of BMSCs (Marked with Cell Tracker CM-DiI, red) and PPM (Labeled with fluorescein isothiocyanate, FITC, green) within the HY. Results indicated that under normal culture conditions, BMSCs were uniformly distributed throughout the HY (Fig. 5F). However, exposure to reactive oxygen species (ROS) significantly reduced the number of BMSCs, leaving only a

few within the HY. The incorporation of PPM effectively protected BMSCs from ROS-induced damage, as evidenced by comparable red fluorescence intensity within the HY compared to the control group. Analysis of cellular proliferation on the first day showed no significant differences among the groups (Fig. 5G). Over time, distinct differences in cellular activity were observed between the HY@PPM and ROS groups. By the seventh day, BMSCs in the ROS environment exhibited minimal activity, while those in the HY@PPM group displayed activity like BMSCs in a normal environment. To assess secretory activity, encapsulated BMSCs were exposed to normal conditions, ROS conditions, and ROS conditions supplemented with PPM. Evaluation of vascular endothelial growth factor (VEGF) secretion in the culture medium revealed no notable difference between the normal and PPM-supplemented groups, but a statistically significant decrease was observed under ROS conditions (Fig. 5H). Notably, the release of MP from HY@PPM reached 83.27 ± 2.65 % at 12 h, which was significantly faster than the secretion of VEGF from HY@PPM&BMSCs. This distinct release profile suggests that the MP can be released first to modulate the microenvironment, creating a more favorable environment for the transplanted BMSCs. These findings underscore the efficacy of HY@PPM in safeguarding BMSCs against adverse microenvironmental conditions, thereby preserving their distribution, viability, and secretory functions

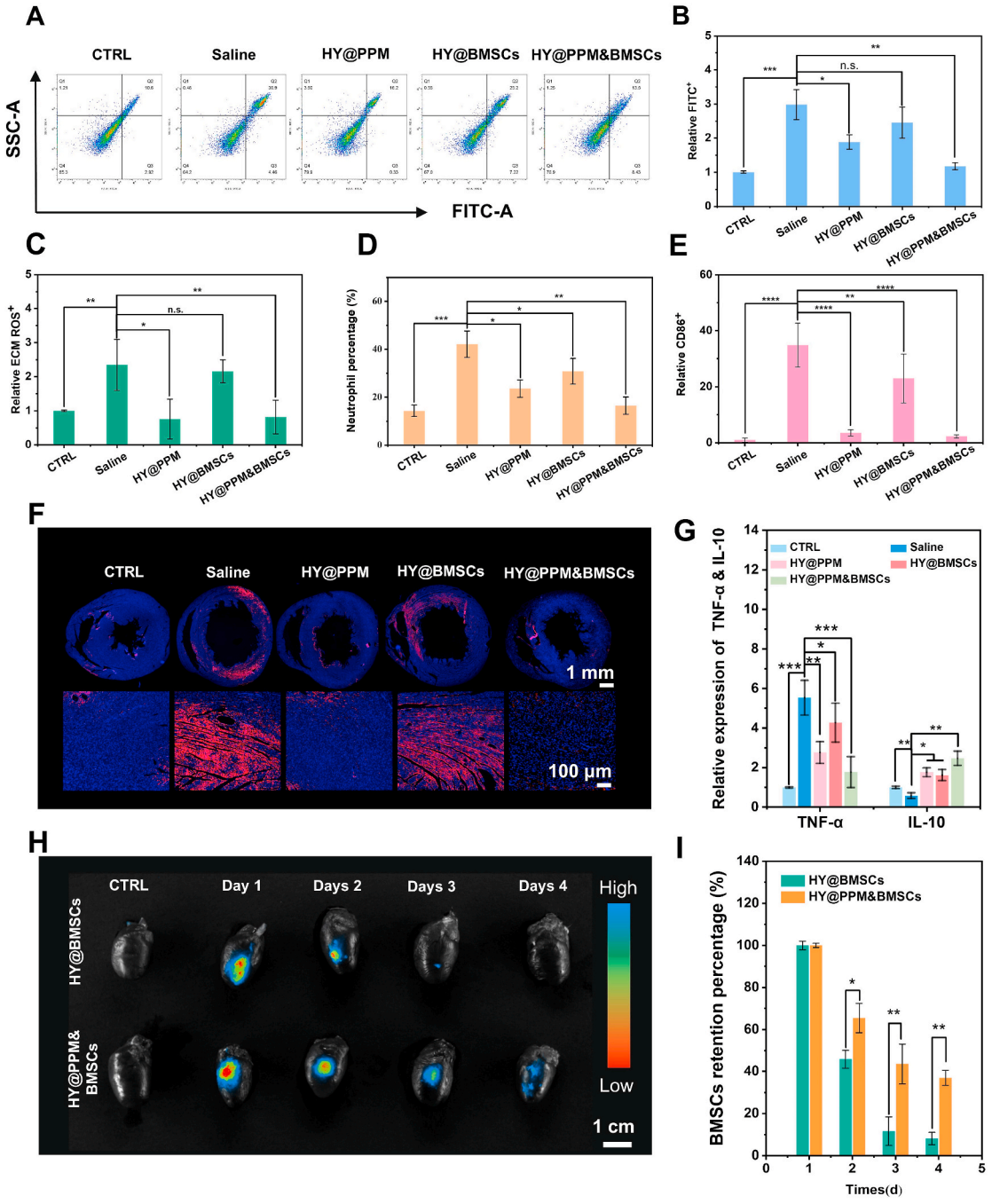

Fig. 6. (A–B) DCFH-DA FC assay and statistics of intracellular ROS in the cardiomyocytes of treated HF rats. (C) ELISA results for ROS in the ECM. (D) Neutrophil percentage in routine blood tests in HF rats after treatment. (E–F) Distribution and statistics of $CD86^{+}$ cells in the heart tissue of HF rats after treatment. (G) Expression levels of TNF-α and IL-10 in cardiac tissues of HF rats after treatment. (H–I) Retention of BMSCs in the pericardium for 1–4 days and statistical analysis. Unless otherwise specified, the relative quantities in the above figures were calculated and statistically analyzed using normal rats as controls.

within the HY.

Furthermore, the Bcl-2-associated X protein (BAX) gene plays a critical role in apoptosis regulation. Overexpression of BAX can antagonize the protective effects of BCL-2, potentially leading to cardiomyocyte apoptosis [53,54]. In this study, BMSCs and H9c2 cells were cocultured in HY and HY@PPM under both normal and challenging conditions. The qPCR analysis revealed that after 1 day of coculture, the expression of the BAX gene in H9c2 cells exposed to the adverse microenvironment increased by 2.54 ± 0.17-fold compared to cells cultured under normal conditions (Fig. 5I). By day 7, expression in the harsh environment rose by 3.58 ± 0.60-fold. Importantly, the introduction of PPM reduced BAX gene expression to 0.32 ± 0.02-fold that of the normal group after 1 day, indicating that HY@PPM effectively protected H9c2 cells in the adverse microenvironment and mitigated apoptotic gene expression.

3.3. PPM-encapsulated HY ameliorates the cardiac microenvironment and prolongs the residence of BMSCs in the pericardium of HF rats

Before commencing animal studies, we conducted assessments on the biocompatibility and safety of HY@PPM&BMSCs through coagulation assays and standard blood analyses (Fig. S3, Table S3). The results confirmed satisfactory blood compatibility of the HY. Following this safety evaluation, heart failure (HF) was induced in rats using intraperitoneal administration of doxorubicin, a method known for its effectiveness in establishing a model of cardiac dysfunction.

Subsequently, a 28-day treatment regimen using the HY@PPM&BMSCs was initiated to evaluate its therapeutic impact on cardiac repair. To analyze changes in intra- and extracellular ROS levels pre- and post-treatment, fresh myocardium homogenates were labeled with DCFH-DA, and ROS levels in the extracellular matrix were assessed. Findings revealed that intracellular ROS levels in the saline group increased by 2.98 ± 0.43-fold compared to the control group, indicating increased ROS levels in the HF microenvironment (Fig. 6A and B). In contrast, intracellular ROS levels in the HY@PPM and HY@PPM&BMSC groups were significantly reduced by 1.88 ± 0.21-fold and 1.17 ± 0.10-fold, respectively. Compared with those in the saline group, the delivery of BMSCs alone did not significantly affect intracellular ROS levels, suggesting that BMSCs have a limited impact on intracellular ROS. However, the codelivery of BMSCs with PPM in the HY@PPM&BMSCs group was significantly different from that in the HY@PPM group, indicating that BMSCs may have a protective effect on intracellular oxidative stress. However, this function may be compromised in adverse microenvironments, limiting effective protection of cardiomyocytes. Results from the extracellular ROS level assay indicated no statistically significant difference in ECM ROS levels between treatment groups containing PPM and the control group (Fig. 6C).

However, ECM ROS levels in the HY@PPM and HY@PPM&BMSCs groups were 0.76 ± 0.58-fold and 0.82 ± 0.49-fold lower than those in the control group, respectively. In contrast, both the saline and HY@BMSCs groups showed increased ECM ROS levels, reaching 2.35 ± 0.75 and 2.16 ± 0.33 times that of the normal group, respectively, with no statistically significant difference between them. Overall, PPM effectively reduced free radicals in both intra- and extracellular microenvironments. While BMSCs impacted intracellular ROS levels and mitigated high ROS conditions, their effectiveness was limited by the adverse microenvironment, hindering their ability to fully reduce intracellular ROS levels. In contrast, PPM scavenged free ROS in the ECM, indirectly lowering intracellular ROS levels and enhancing BMSCs' capability to improve intracellular ROS levels in cardiomyocytes. Notably, the enhancement of intracellular ROS in cardiomyocytes by BMSCs occurred through their paracrine effects on oxidative stress-related pathways rather than direct ROS scavenging. This underscores that BMSCs may modulate changes in intracellular ROS levels via paracrine signaling. Changes in inflammation-related markers were monitored through routine blood tests. Meanwhile, the percentage of neutrophils in the saline group was significantly greater than that in the normal group, reaching 40.03 ± 10.51 %, whereas the percentage in the PPM treatment group decreased by 23.55 ± 3.60 %, which was significantly different from that in the saline group (Fig. 6D). This observation suggested that PPM effectively attenuated inflammation. A comparable decrease was noted in the BMSC group, with a percentage of 30.80 ± 5.35 %, although this difference did not reach statistical significance compared to the saline group, indicating that BMSCs had a limited impact on reducing inflammation (the normal range of neutrophil percentage in rats is 7.30–30.10 %). To further evaluate local inflammation changes pre- and post-treatment, cardiac tissue was sectioned and subjected to CD86 immunofluorescence staining. CD86, found on immune cell surfaces, plays a role in activating various inflammatory pathways. The percentage of $CD86^{+}$ cells (red fluorescence) was greater in both the saline treatment group and the HY@BMSCs group, as indicated by intense red fluorescence (Fig. 6E and F).

However, in the groups in which PPM was introduced, including the HY@PPM and HY@PPM&BMSCs groups, the intensity of the red fluorescence signal was significantly lower than that in the normal rat cardiac tissue group. Following this, fresh heart tissues were collected to analyze the expression of TNF-α and IL-10. The results demonstrated that TNF-α expression in cardiac tissues of rats treated with saline was notably higher (7.53 ± 2.88-fold) compared to the normal group (Fig. 6G). In contrast, TNF-α expression in the PPM group showed a reduction of 2.76 ± 1.55-fold compared to the saline group. Similarly, the TNF-α expression in the HY@BMSC group decreased to 4.27 ± 1.98-fold greater than that in the normal group, although this difference was not significant. In the HY@PPM&BMSC group, TNF-α expression was only 1.77 ± 0.78 times greater than that in the normal group and was not significantly different from that in the normal group. In contrast to that in the TNF-α group, the expression of IL-10 in the saline group was 1.17 ± 0.36 times greater, and the relative expression of IL-10 in the HY@PPM, HY@BMSCs, and HY@PPM&BMSCs groups was 0.38 ± 0.14, 0.76 ± 0.22, 0.62 ± 0.28, and 1.17 ± 0.36 times greater, respectively, than that in the normal group.

These results suggest that both PPM and BMSCs hold promise for improving the local inflammatory environment. However, the influence of the microenvironment on BMSCs may limit their ability to regulate macrophage phenotype. Nonetheless, BMSCs have the capacity to influence cytokine secretion to some extent.

Enhancing adverse microenvironment significantly boosts BMSCs retention within the pericardium. To explore how microenvironment improvements affect BMSCs retention post-transplantation, we labeled BMSCs with CM-Dil and tracked their presence in the pericardium. The retention rate of BMSCs in the HY was 45.86 ± 4.31 % on the second day, whereas in the PPM group, it was notably higher at 65.50 ± 6.99 % (Fig. 6H and I), indicating that PPM-driven microenvironmental enhancement substantially enhances stem cell retention. This difference became more pronounced over time, with BMSCs in the HY group decreasing to 8.13 ± 2.94 % by the fourth day, while those in the PPM-incorporated HY group remained at 36.95 ± 3.58 %. These findings underscore that embedding BMSCs in a HY matrix enriched with PPM can minimize BMSC loss and extend their residency in the pericardium.

3.4. Therapeutic effect of HY@PPM&BMSCs on HF rats

Histological analysis using H&E staining revealed that the ventricular wall was visibly thinner in the saline group compared to the control group (Fig. 7A and B). Additionally, there was a notable increase in interstitial space between cardiomyocytes, indicating structural changes in the heart that compressed the normal left ventricle space. In contrast, rats in the HY@PPM group showed signs of ventricular wall recovery, although gaps between tissues were still evident. The cardiac structure of the HY@BMSCs and HY@PPM&BMSCs groups was restored to a level similar to the normal group, exhibiting denser and more structurally

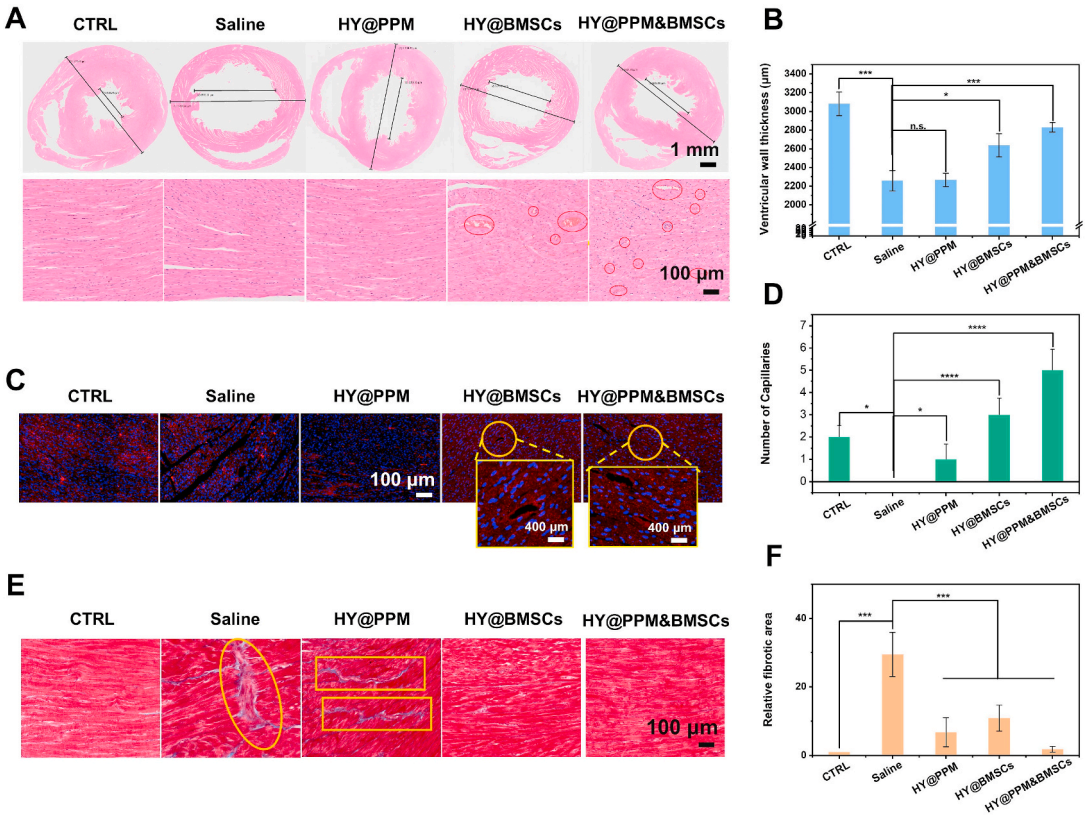

Fig. 7. (A) H&E staining of heart tissue from treated HF rats. (B) Statistical analysis of ventricular wall thickness. (C) CD31 (red) staining of rat heart tissue slices after treatment. (D) Random statistics of the number of new blood vessels (n = 6). (E) Masson staining of cardiac tissue. (F) Statistics of the relative fibrotic area (calculated using normal rats as a control).

intact cardiac tissue. Detailed section magnifications revealed that BMSCs implantation significantly increased the number of interstitial capillaries, characterized by a ring-like shape, with visible accumulation of red blood cells within these vessels (Fig. 7C and D). These results suggest that BMSC implantation contributed to the recovery of injured cardiac tissues and enhanced the microenvironment, further augmenting the tissue recovery effects of BMSCs. This enhancement is likely linked to the prolonged retention of BMSCs within the pericardium.

Cardiac injury often results in ventricular remodeling and fibrosis, which can significantly impair normal heart function. Masson staining was used to examine cardiac structural alterations and fibrosis, and intercellular fibrotic areas were randomly counted to assess these changes. In the saline group, there was extensive fibrotic tissue (blue) and a less dense ventricular structure with increased intercellular spaces compared to the normal group (Fig. 7E). However, in the PPM-incorporated HY group, the fibrotic area was reduced relative to the saline group, though intercellular spaces remained larger than those in the normal group. The HY@BMSCs group exhibited significant improvement in tissue structure, showing a distinct reduction in the fibrotic area compared to the saline group (Fig. 7F), despite denser intercellular spaces and some cells displaying poor morphology. In contrast, the HY@PPM&BMSCs group displayed tissue structure similar to the control group, suggesting that BMSCs facilitated the recovery of damaged tissues and that PPM effectively enhanced the therapeutic effect of BMSCs.

Annexin V-FITC staining (green fluorescence) was utilized to assess apoptosis in cardiac tissue sections, using normal mouse hearts as controls. The saline-treated group exhibited a significant increase in apoptosis, with the apoptotic fluorescence signal being 55.88 ± 9.67 times higher than that in the normal group (Fig. 8A and B). However, the inclusion of PPM and BMSCs resulted in reduced cardiomyocyte apoptosis. In the group treated with PPM-incorporated HY, the fluorescence intensity of apoptotic cells decreased to 12.95 ± 7.03 times that of the control group, which was significantly lower than that in the saline group. This improvement can be attributed to the PPM's effect on altering the microenvironment. The impact of HY-encapsulated BMSCs on apoptosis was even more pronounced, with apoptotic fluorescence decreasing to 4.60 ± 1.63 times that of the control group. Furthermore, PPM prolonged the retention time of BMSCs, leading to a further reduction in the percentage of apoptotic cells in the HY-encapsulated PPM and BMSC group to 1.82 ± 1.35-fold, a value not significantly different from that in the normal group.

To evaluate cardiac function before and after treatment, rats were anesthetized and underwent cardiac ultrasound to measure the left ventricular ejection fraction (LVEF), a critical indicator of heart pumping efficiency. The results indicated that LVEF decreased to 41.27 ± 2.44 % in rats with HF (Fig. 8C and D), confirming the successful establishment of the HF model. However, no significant difference in cardiac ejection capacity was observed between the saline-treated, HY@PPM-treated, and HF groups, suggesting that PPM improved the injured microenvironment, it did not significantly affect cardiac function recovery. In contrast, LVEF in the HY@BMSCs group increased to 64.56 ± 3.04 %, signifying a notable role in promoting cardiac function recovery. Moreover, LVEF in the HY@PPM&BMSC group further rose to 80.56 ± 3.20 %, demonstrating substantial improvement in cardiac ejection capacity, albeit still below that of the normal group (91.46 ± 3.46 %). Similarly, the fraction shortening (FS) in the HY@PPM&BMSCs group further increased to 57.07 ± 6.69 % compared with that in the HF group (22.64 ± 2.43 %) and saline group (19.26 ± 4.22 %) (Fig. 8E). The combination of PPM with BMSCs to improve the microenvironment significantly enhanced the therapeutic efficacy of BMSCs, emphasizing the importance of microenvironmental improvement in successful treatment. In conclusion, PPM itself did not directly impact cardiac function recovery, BMSCs displayed promising potential for treating HF,

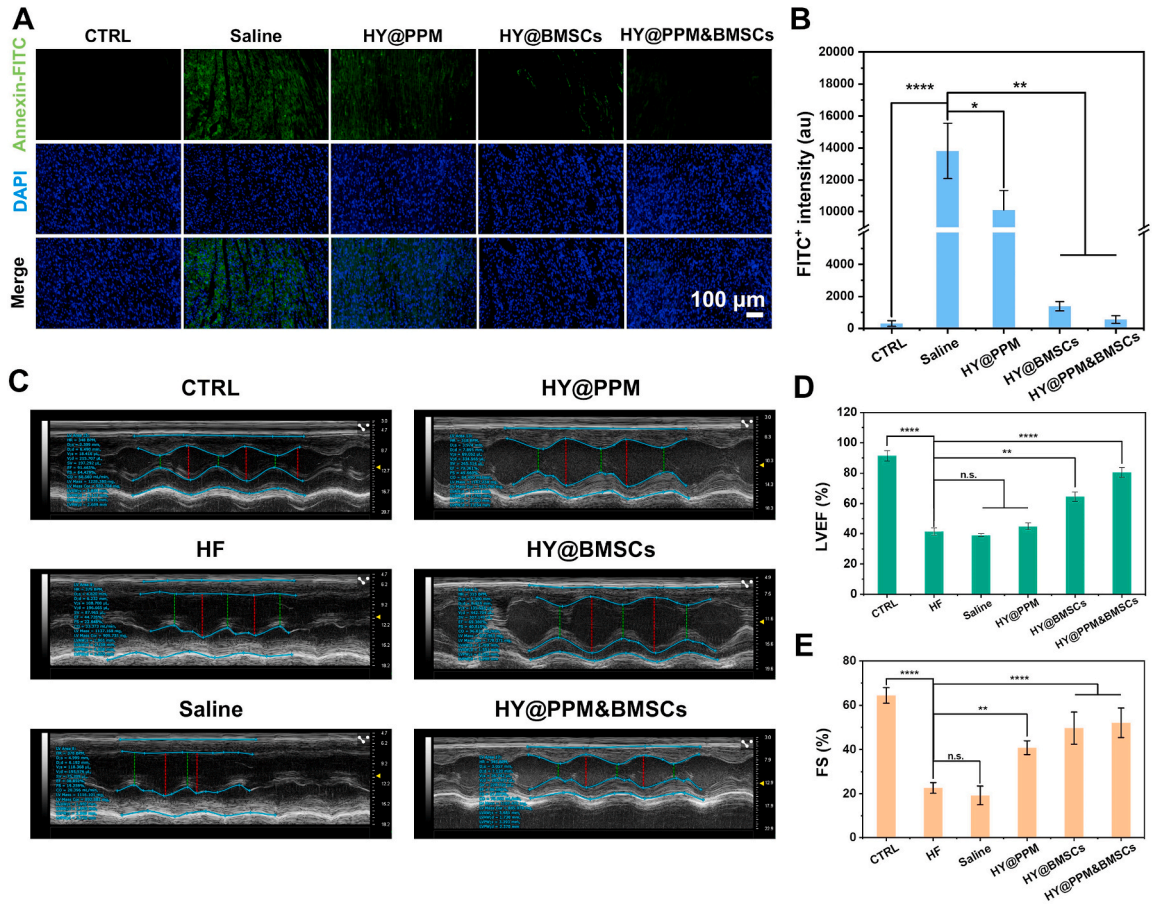

Fig. 8. (A–B) Annexin-FITC (Green) staining of cardiac tissue slices and statistical analysis of myocardial cell apoptosis. (C) Echocardiographic evaluation of left ventricular function. (D) The LVEF of normal rats and treated HF rats. (E) The FS of normal rats and treated HF rats.

greatly benefiting from the enhanced microenvironment facilitated by PPM.

Despite the progress made in this study to enhance the *in vivo* residence time of BMSCs, there are still several limitations. In *in vitro* experiments, we observed that BMSCs maintained over 80 % cellular viability for up to 7 days of co-culture with H9c2 cells. However, *in vivo* results showed that intrapericardial retention dropped to under 40 % after 4 days. This discrepancy may be attributed to the continuous beating of the heart, which could accelerate the degradation of the hydrogel and lead to the leakage and subsequent clearance of BMSCs into the pericardial tissue. Additionally, challenges related to the acquisition and cultivation of BMSCs, as well as their inter-individual variability, also limited the scope for further in-depth exploration in this study.

4. Conclusion

In summary, this study introduces a novel way of BMSCs transplantation, using PPM to enhance the survival and function of transplanted BMSCs for treating HF. All experiments in this study have shown that this assisted transplantation protocol for BMSCs is safe and effective. Firstly, PPM not only scavenged ROS but also polarized macrophages from the pro-inflammatory M1 phenotype to the pro-regenerative M2 phenotype, restoring a conducive microenvironment for BMSCs. Notably, this restoration significantly improved the survival and secretion activity of BMSCs in an adverse microenvironment. After 24 h, a retention rate of 65.50 ± 6.99 % was observed, and a substantial retention rate of 36.99 ± 3.58 % was still maintained after 96 h. While the 24 h retention rate in many previous studies was no more than 50 %. The efficacy of HY@PPM&BMSCs was evaluated in HF rat models, where it successfully restored the inflammatory microenvironment in the pericardium, leading to significant reductions in ROS and pro-inflammatory cytokine. Consequently, enhanced survival of transplanted BMSCs was observed in HF rat models, accompanied by improvements in cardiac function. These findings provide valuable insights for advancing BMSCs-based therapies for HF and their potential clinical applications.

Ethics approval and consent to participate

All animal experiments were approved by Medical Ethics Committee of The third people's hospital of Chengdu (AWEC Issue No. CDTPH2023061201).

CRediT authorship contribution statement

Tian Yue: Writing – original draft, Methodology, Investigation, Formal analysis, Conceptualization. **Wentai Zhang:** Writing – review & editing, Methodology, Investigation, Conceptualization. **Haifeng Pei:** Writing – review & editing, Methodology, Formal analysis. **Dunzhu Danzeng:** Writing – review & editing, Supervision, Methodology. **Jian He:** Writing – original draft, Investigation, Data curation. **Jiali Yang:** Writing – review & editing, Methodology, Investigation. **Yong Luo:** Writing – review & editing, Methodology. **Zhen Zhang:** Supervision, Conceptualization. **Shiqiang Xiong:** Validation, Investigation. **Xiangbo Yang:** Resources, Investigation. **Qisen Ji:** Resources, Investigation. **Zhilu Yang:** Writing – review & editing, Supervision, Methodology, Funding acquisition, Formal analysis, Conceptualization. **Jun Hou:**

Writing – review & editing, Supervision, Methodology, Funding acquisition, Formal analysis, Conceptualization.

Declaration of competing interest

The authors declare the following personal relationships which may be considered as potential competing interests: Zhilu Yang is an editorial board member for Bioactive Materials and was not involved in the editorial review or the decision to publish this article. Xiangbo Yang and Qisen Ji are currently employed by Ya'an Xunkang Pharmaceutical Co., LTD.

Acknowledgements

This work was supported by the National Natural Science Foundation of China (81900339, 82072072, 32261160372), The Third People's Hospital of Chengdu First-Class Incubation Project (CSY-YN-01-2023-003), Special Funding for Postdoctoral Research in Sichuan Province (2023TB095), The Fundamental Research Funds for the Central Universities (2682022TPY052), Chengdu Medical Research Project (2022138), and the Natural Science Foundation of Tibet Autonomous Region Grant number (XZ202201ZR0036G).

Appendix A. Supplementary data

Supplementary data to this article can be found online at https://doi.org/10.1016/j.bioactmat.2024.08.038.

References

[1] P.A. Heidenreich, B. Bozkurt, D. Aguilar, L.A. Allen, J.J. Byun, M.M. Colvin, A. Deswal, M.H. Drazner, S.M. Dunlay, L.R. Evers, J.C. Fang, S.E. Fedson, G. C. Fonarow, S.S. Hayek, A.F. Hernandez, P. Khazanie, M.M. Kittleson, C.S. Lee, M. S. Link, C.A. Milano, L.C. Nnacheta, A.T. Sandhu, L.W. Stevenson, O. Vardeny, A. R. Vest, C.W. Yancy, AHA/ACC/HFSA guideline for the management of heart failure: a report of the American college of cardiology/American heart association joint committee on clinical practice Guidelines, Circulation 145 (18) (2022) e895–e1032, 2022.

[2] B.A. Borlaug, K. Sharma, S.J. Shah, J.E. Ho, Heart failure with preserved ejection fraction: JACC scientific statement, J. Am. Coll. Cardiol. 81 (18) (2023) 1810–1834.

[3] M.M. Redfield, B.A. Borlaug, Heart failure with preserved ejection fraction: a review, JAMA 329 (10) (2023) 827–838.

[4] J. Ren, H.W. Li, L. Chen, M. Zhang, Y.X. Liu, B.W. Zhang, R. Xu, Y.Y. Miao, X. M. Xu, X. Hua, X.G. Sun, R.J. Yu, Y.T. Long, S.S. Hu, Mass Spectrometry Imaging-Based Single-Cell Lipidomics Profiles Metabolic Signatures of Heart Failure, vol. 6, Research (Wash D C), 2023, p. 19.

[5] X. Song, J. Zhang, S. Shen, D. Liu, J. Zhang, W. Yin, G. Ye, L. Wang, L. Cai, H. Hou, X. Qiu, Cardiac-Adaptive Conductive Hydrogel Patch Enabling Construction of Mechanical-Electrical Anisotropic Microenvironment for Heart Repair, vol. 6, Research (Wash D C), 2023, p. 161.

[6] J.C. Garbern, R.T. Lee, Heart regeneration: 20 years of progress and renewed optimism, Dev. Cell 57 (4) (2022) 424–439.

[7] J.T. Willerson, The medical and device-related treatment of heart failure, Circ. Res. 124 (11) (2019) 1519.

[8] E. Akwo, M.M. Pike, L.A. Ertuglu, N. Vartanian, E. Farber-Eger, L. Lipworth, F. Perwad, E. Siew, A. Hung, N. Bansal, I. de Boer, B. Kestenbaum, N.J. Cox, T. A. Ikizler, Q. Wells, C. Robinson-Cohen, Association of genetically predicted fibroblast growth factor-23 with heart failure: a mendelian randomization study, Clin. J. Am. Soc. Nephrol. 17 (8) (2022) 1183–1193.

[9] P. Menasché, Mesenchymal stromal cell therapy for heart failure: never stop DREAMing, J. Am. Coll. Cardiol. 81 (9) (2023) 864–866.

[10] B. Ratner, Vascular grafts: Technology success/technology failure, BME Front 4 (2023) 3.

[11] R. Bolli, M. Solankhi, X.L. Tang, A. Kahlon, Cell therapy in patients with heart failure: a comprehensive review and emerging concepts, Cardiovasc. Res. 118 (4) (2022) 951–976.

[12] J. Zou, W. Yang, W. Cui, C. Li, C. Ma, X. Ji, J. Hong, Z. Qu, J. Chen, A. Liu, H. Wu, Therapeutic potential and mechanisms of mesenchymal stem cell-derived exosomes as bioactive materials in tendon-bone healing, J. Nanobiotechnol. 21 (1) (2023) 14.

[13] K. Matsushita, Heart failure and adipose mesenchymal stem cells, Trends Mol. Med. 26 (4) (2020) 369–379.

[14] X. Zhao, W. Zhang, J. Fan, X. Chen, X. Wang, Application of mesenchymal stem cell exosomes in the treatment of skin wounds, Smart Mater. Med. 4 (2023) 578–589.

[15] W. Xiong, R. Zhang, H. Zhou, Y. Liu, M. Liang, K. Li, X. Duan, D.P. Chen, Y. Luo, J. Xu, Y. Ai, Y. He, Q. Ye, Application of nanomedicine and mesenchymal stem cells in burn injuries for the elderly patients, Smart Mater. Med. 4 (2023) 78–90.

[16] H. Amini, A.R. Namjoo, M.T. Narmi, N. Mardi, S. Narimani, O. Naturi, N. D. Khosrowshahi, R. Rahbarghazi, S. Saghebasl, S. Hashemzadeh, M. Nouri, Exosome-bearing hydrogels and cardiac tissue regeneration, Biomater. Res. 27 (1) (2023) 99.

[17] C. Zhao, S. Tian, Q. Liu, K. Xiu, I. Lei, Z. Wang, P.X. Ma, Biodegradable nanofibrous temperature-responsive gelling microspheres for heart regeneration, Adv. Funct. Mater. 30 (21) (2020).

[18] G. Choe, S.W. Kim, J. Park, J. Park, S. Kim, Y.S. Kim, Y. Ahn, D.W. Jung, D. R. Williams, J.Y. Lee, Anti-oxidant activity reinforced reduced graphene oxide/alginate microgels: mesenchymal stem cell encapsulation and regeneration of infarcted hearts, Biomaterials 225 (2019) 119513.

[19] R. Madonna, L.W. Van Laake, H.E. Botker, S.M. Davidson, R. De Caterina, F. B. Engel, T. Eschenhagen, F. Fernandez-Aviles, D.J. Hausenloy, J.S. Hulot, S. Lecour, J. Leor, P. Menasché, M. Pesce, C. Perrino, F. Prunier, S. Van Linthout, K. Ytrehus, W.H. Zimmermann, P. Ferdinandy, J.P.G. Sluijter, ESC Working Group on Cellular Biology of the Heart, Position paper for Cardiovascular Research: tissue engineering strategies combined with cell therapies for cardiac repair in ischaemic heart disease and heart failure, Cardiovasc. Res. 115 (3) (2019) 488–500.

[20] Z. Wu, L. Fan, C. Chen, Y. Ma, X. Wu, Y. Li, Z. Hao, T. Yang, Promotion of osteoporotic bone healing by a tannic acid modified strontium-doped biomimetic bone lamella with ROS scavenging capacity and pro-osteogenic effect, Smart Mater. Med. 4 (2023) 590–602.

[21] G.V. Halade, D.H. Lee, Inflammation and resolution signaling in cardiac repair and heart failure, EBioMedicine 79 (2022) 103992.

[22] L. Adamo, C. Rocha-Resende, S.D. Prabhu, D.L. Mann, Reappraising the role of inflammation in heart failure, Nat. Rev. Cardiol. 17 (5) (2020) 269–285.

[23] J. Zhou, C. Fang, C. Rong, T. Luo, J. Liu, K. Zhang, Reactive oxygen species-sensitive materials: a promising strategy for regulating inflammation and favoring tissue regeneration, Smart Mater. Med. 4 (2023) 427–446.

[24] D. Weissman, C. Maack, Redox signaling in heart failure and therapeutic implications, Free Radic. Biol. Med. 171 (2021) 345–364.

[25] H. Sies, V.V. Belousov, N.S. Chandel, M.J. Davies, D.P. Jones, G.E. Mann, M. P. Murphy, M. Yamamoto, C. Winterbourn, Defining roles of specific reactive oxygen species (ROS) in cell biology and physiology, Nat. Rev. Mol. Cell Biol. 23 (7) (2022) 499–515.

[26] J. Zhang, D. Sun, Y. Liao, B. Cao, R. Gao, Z. Zeng, C. Zheng, Y. Wei, X. Guo, Time-released black phosphorus hydrogel accelerates myocardial repairing through antioxidant and motivates macrophage polarization properties, Biomater. Res. 28 (2024) 29.

[27] W. Zhang, X. Dai, X. Jin, M. Huang, J. Shan, X. Chen, H. Qian, Z. Chen, X. Wang, Promotion of wound healing by a thermosensitive and sprayable hydrogel with nanozyme activity and anti-inflammatory properties, Smart Mater. Med. 4 (2023) 134–145.

[28] J. Tang, X. Cui, T.G. Caranasos, M.T. Hensley, A.C. Vandergriff, Y. Hartanto, D. Shen, H. Zhang, J. Zhang, K. Cheng, Heart repair using nanogel-encapsulated human cardiac stem cells in mice and pigs with myocardial infarction, ACS Nano 11 (10) (2017) 9738–9749.

[29] Y. Chen, C. Li, C. Li, J. Chen, Y. Li, H. Xie, C. Lin, M. Fan, Y. Guo, E. Gao, W. Yan, L. Tao, Tailorable hydrogel improves retention and cardioprotection of intramyocardial transplanted mesenchymal stem cells for the treatment of acute myocardial infarction in mice, J. Am. Heart Assoc. 9 (2) (2020) e013784.

[30] B. Zhang, X. Zhang, K. Wan, J. Zhu, J. Xu, C. Zhang, T. Liu, Dense Hydrogen-Bonding Network Boosts Ionic Conductive Hydrogels with Extremely High Toughness, Rapid Self-Recovery, and Autonomous Adhesion for Human-Motion Detection, vol. 2021, Research (Wash D C), 2021 9761625.

[31] G. Huang, H. Shen, K. Xu, Y. Shen, J. Jiale, G. Chu, H. Xing, Z. Feng, Y. Wang, Single-Cell Microgel Encapsulation Improves the Therapeutic Efficacy of Mesenchymal Stem Cells in Treating Intervertebral Disc Degeneration via Inhibiting Pyroptosis, vol. 7, Research (Wash D C), 2024, p. 311.

[32] W. Liu, N. Zhao, Q. Yin, X. Zhao, K. Guo, Y. Xian, S. Li, C. Wang, M. Zhu, Y. Du, F. J. Xu, C. Wang, J. Zhou, Injectable hydrogels encapsulating dual-functional Au@Pt core-shell nanoparticles regulate infarcted microenvironments and enhance the therapeutic efficacy of stem cells through antioxidant and electrical integration, ACS Nano 17 (3) (2023) 2053–2066.

[33] Y. You, K. Kobayashi, B. Colak, P. Luo, E. Cozens, L. Fields, K. Suzuki, J. Gautrot, Engineered cell-degradable poly(2-alkyl-2-oxazoline) hydrogel for epicardial placement of mesenchymal stem cells for myocardial repair, Biomaterials 269 (2021) 120356.

[34] M. Kasravi, A. Ahmadi, A. Babajani, R. Mazloomnejad, M.R. Hatamnejad, S. Shariatzadeh, S. Bahrami, H. Niknejad, Immunogenicity of decellularized extracellular matrix scaffolds: a bottleneck in tissue engineering and regenerative medicine, Biomater. Res. 27 (1) (2023) 10.

[35] L. Chen, S. Li, J. Zhu, A. You, X. Huang, X. Yi, M. Xue, Mangiferin prevents myocardial infarction-induced apoptosis and heart failure in mice by activating the Sirt1/FoxO3a pathway, J. Cell Mol. Med. 25 (6) (2021) 2944–2955.

[36] S.H. Wang, K.L. Tsai, W.C. Chou, H.C. Cheng, Y.T. Huang, H.C. Ou, Y.C. Chang, Quercetin mitigates cisplatin-induced oxidative damage and apoptosis in cardiomyocytes through Nrf2/HO-1 signaling pathway, Am. J. Chin. Med. 50 (5) (2022) 1281–1298.

[37] T. Jiang, F. Han, G. Gao, M. Liu, Mangiferin exert cardioprotective and anti-apoptotic effects in heart failure induced rats, Life Sci. 249 (2020) 117476.

[38] N. Baheiraei, M. Razavi, R. Ghahremanzadeh, Reduced graphene oxide coated alginate scaffolds: potential for cardiac patch application, Biomater. Res. 27 (1) (2023) 109.
[39] S.J. Feng, Z.H. Tang, Y. Wang, X.Y. Tang, T.H. Li, W. Tang, Z.M. Kuang, Potential protective effects of red yeast rice in endothelial function against atherosclerotic cardiovascular disease, Chin. J. Nat. Med. 17 (1) (2019) 50–58.
[40] D. Choe, S.M. Song, C.S. Shin, T.V. Johnston, H.J. Ahn, D. Kim, S. Ku, Production and characterization of anti-inflammatory monascus pigment derivatives, Foods 9 (7) (2020).
[41] S. Ning, C. Wang, L. Zhao, J. Yang, X. Shi, Y. Zheng, Lecithin/chitosan nanoparticle drug carrier improves anti-tumor efficacy of Monascus pigment rubropunctatin, Int. J. Biol. Macromol. 242 (Pt 3) (2023) 125058.
[42] Z. Jiang, S. Qin, W. Wang, T. Du, Y. Zang, Y. He, X. Dong, H. Liu, G. Ma, Investigating the anti-inflammatory and bone repair-promoting effects of an injectable porous hydrogel containing magnesium ions in a rat periodontitis mode, Smart Mater. Med. 5 (2) (2024) 207–220.
[43] Z. Yuan, L. Zhang, S. Jiang, M. Shafiq, Y. Cai, Y. Chen, J. Song, X. Yu, H. Ijima, Y. Xu, Anti-inflammatory, antibacterial, and antioxidative bioactive glass-based nanofibrous dressing enables scarless wound healing, Smart Mater. Med. 4 (2023) 407–426.
[44] Y.-T. Lu, P.-T. Hung, K. Zeng, C. Woelk, B. Fuhrmann, K. Zhang, T. Groth, Surface properties and bioactivity of PNIPAM-grafted-chitosan/chondroitin multilayers, Smart Mater. Med. 4 (2023) 356–367.
[45] Y. Fan, L. Liang, X. Tang, J. Zhu, L. Mu, M. Wang, X. Huang, S. Gong, J. Xu, T. Liu, T. Zhang, Changes in the gut microbiota structure and function in rats with doxorubicin-induced heart failure, Front. Cell. Infect. Microbiol. 13 (2023) 1135428.
[46] T. Ding, S. Wang, X. Zhang, W. Zai, J. Fan, W. Chen, Q. Bian, J. Luan, Y. Shen, Y. Zhang, D. Ju, X. Mei, Kidney protection effects of dihydroquercetin on diabetic nephropathy through suppressing ROS and NLRP3 inflammasome, Phytomedicine 41 (2018) 45–53.
[47] Q. Chen, Q. Li, Y. Liang, M. Zu, N. Chen, B.S.B. Canup, L. Luo, C. Wang, L. Zeng, B. Xiao, Natural exosome-like nanovesicles from edible tea flowers suppress metastatic breast cancer via ROS generation and microbiota modulation, Acta Pharm. Sin. B 12 (2) (2022) 907–923.
[48] W. Chen, M. Schilperoort, Y. Cao, J. Shi, I. Tabas, W. Tao, Macrophage-targeted nanomedicine for the diagnosis and treatment of atherosclerosis, Nat. Rev. Cardiol. 19 (4) (2022) 228–249.
[49] Y. Hayashi, M. Takamiya, P.B. Jensen, I. Ojea-Jimenez, H. Claude, C. Antony, K. Kjaer-Sorensen, C. Grabher, T. Boesen, D. Gilliland, Differential nanoparticle sequestration by macrophages and scavenger endothelial cells visualized in vivo in real-time and at ultrastructural resolution, ACS Nano 14 (2) (2020) 1665–1681.
[50] Y. Liu, M. Wu, C. Zhong, B. Xu, L. Kang, M2-like macrophages transplantation protects against the doxorubicin-induced heart failure via mitochondrial transfer, Biomater. Res. 26 (1) (2022) 14.
[51] Q. Sun, H. Ma, J. Zhang, B. You, X. Gong, X. Zhou, J. Chen, G. Zhang, J. Huang, Q. Huang, Y. Yang, K. Ai, Y. Bai, A self-sustaining antioxidant strategy for effective treatment of myocardial infarction, Adv. Sci. 10 (5) (2023) e2204999.
[52] J. Zhou, W. Liu, X. Zhao, Y. Xian, W. Wu, X. Zhang, N. Zhao, F.J. Xu, C. Wang, Natural melanin/alginate hydrogels achieve cardiac repair through ROS scavenging and macrophage polarization, Adv. Sci. 8 (20) (2021) e2100505.
[53] Q. Tang, H. Chen, Z. Mai, H. Sun, L. Xu, G. Wu, Z. Tu, X. Cheng, X. Wang, T. Chen, Bim- and Bax-mediated mitochondrial pathway dominates abivertinib-induced apoptosis and ferroptosis, Free Radic. Biol. Med. 180 (2022) 198–209.
[54] H. Flores-Romero, L. Hohorst, M. John, M.C. Albert, L.E. King, L. Beckmann, T. Szabo, V. Hertlein, X. Luo, A. Villunger, L.P. Frenzel, H. Kashkar, A.J. Garcia-Saez, BCL-2-family protein tBID can act as a BAX-like effector of apoptosis, EMBO J. 41 (2) (2022) e108690.